

Mass and energy balance calculations for artificial ice reservoirs (Icestupas)

Suryanarayanan Balasubramanian^{1*}, Martin Hoelzle¹, Michael Lehning²,
Sonam Wangchuk³, Johannes Oerlemans⁴, Felix Keller^{5,6} and Jordi Bolíbar⁴

¹ University of Fribourg, Fribourg, Switzerland

² WSL Institute for Snow and Avalanche Research, Davos, Switzerland

³ Himalayan Institute of Alternatives Ladakh, Leh, India

⁴ Institute for Marine and Atmospheric Research, Utrecht University, Utrecht, The Netherlands

⁵ Academia Engiadina, Samedan, Switzerland

⁶ ETH, Zürich, Switzerland

Correspondence*:

Suryanarayanan Balasubramanian

suryanarayanan.balasubramanian@unifr.ch

2 ABSTRACT

Artificial Ice Reservoirs (AIRs) can successfully store water during winter and release the water during spring and summer. This makes them a reliable fresh water resource for irrigation in dry environments. Several AIRs have been built but studies of their water storage capacity and efficiency are scarce. This study models a cone-shaped AIR popularly called Icestupa. Processes involved in the development and temporal evolution of an Icestupa are calculated by a physically-based model using equations governing the heat transfer, vapour diffusion and transport of water that undergoes phase changes. These processes were quantified using meteorological data in conjunction with fountain spray information (mass input of an AIR) to estimate the quantity of frozen, melted, evaporated and runoff water for three sites in Switzerland and one in India. At these measurement sites, AIR were built for model validation purposes. The model was further tested by performing a sensitivity and uncertainty study showing that the most sensitive parameters are the ice emissivity and the temperature threshold used to determine precipitation phase. Model calculations estimate that the AIR stored about % of the total water sprayed as ice.

Keywords: iceshelf, mass balance, water storage, climate change adaptation, geoengineering

1 INTRODUCTION

Seasonal snow cover, glaciers and permafrost are expected to change their water storage capacity due to climate change with major consequences for downriver water supply (Immerzeel et al., 2019). The challenges brought about by these changes are especially important for dry mountain environments such as in Central Asia or the Andes, which directly rely on the seasonal meltwater for their farming and drinking needs (Hoelzle et al., 2019; Apel et al., 2018; Buytaert et al., 2017; Chen et al., 2016; Unger-Shayesteh et al., 2013). Some villages in Ladakh, India have already been forced to relocate due to glacial retreat and the corresponding loss of their main fresh water resources (Grossman, 2015).



Figure 1. Icestupa in Ladakh, India on March 2017 was 24 m tall and contained around 3700 m³ of water.
Picture Credits: Lobzang Dadul

24 Artificial ice reservoirs (AIRs) have been considered to be a feasible way to adapt to these changes (Hock
25 et al., 2019; Nüsser et al., 2019b). An AIR is a human-made ice structure typically constructed during the
26 cold winter months and designed to slowly release freshwater during the warm and dry spring and summer
27 months. The main purpose of AIRs is irrigation. Therefore, AIRs are designed to store water in the form of
28 ice as long into the summer as possible. The energy required to construct an AIR is usually derived from
29 the gravitational head of the source water body. Some are constructed horizontally by freezing water using
30 a series of checkdams and others are built vertically by spraying water through fountain systems (Nüsser
31 et al., 2019a). The latter are colloquially referred to as Icestupas and are the subject of this study.

32 A typical Icestupa just requires a pipeline attached to a vertically mounted metal pipe with a fountain
33 nozzle for construction. Their water source is usually a high altitude lake or glacial stream. Due to the
34 altitude difference between the pipeline input and fountain output, water ejects from the fountain nozzle as
35 droplets that eventually lose their latent heat to the atmosphere and accumulate as ice around the metal pipe.
36 The fountain nozzle is raised through addition of further pipes as and when significant ice accumulates.
37 Typically, a dome of branches is constructed around the metal pipe so that such pipe extensions can be
38 done from within this dome. During the winter, the fountain is manually activated from sunset to sunrise.
39 Threads, tree branches and fishing nets are used to guide and accelerate the ice formation.

40 Since their invention in 2013 (Wangchuk, 2014), Icestupas have gained widespread publicity in the region
41 of Ladakh, Northern India since they require very little infrastructure, skills and energy to be constructed
42 in comparison to other water storage technologies. Compared to other AIR geometries, Icestupas (Fig.
43 1) can be built at lower altitudes and last much longer into the summer than other types of ice structures
44 (Wangchuk, 2014). However, to date, no reliable estimates exist about the amount of sprayed water that
45 is necessary to create them and the meltwater they provide (Nüsser et al., 2019a). Rough estimates of
46 Icestupa meltwater in Ladakh suggest that the water loss during the construction process is considerable
47 (see Appendix 6.1). A complete set of measurements of the water storage and energy balance are required
48 to understand the cause of the water losses better and increase the construction efficiency.

49 In this paper, we aim to develop a physically-based model of a vertical AIR (or Icestupa) that can quantify
50 their storage efficiency using existing weather and water usage information. Mass and energy balance

equations were used to estimate the quantity of water frozen, melted, evaporated and runoff. Sensitivity and uncertainty analysis were performed to identify the most critical parameters and the variance caused by them. For validation, we chose four AIR built across the winters of 2019, 2020 and 2021 in India and Switzerland. Our model and validation experiments provide first steps towards evaluating the effectiveness of a vertical AIR for irrigation and allow us to outline some preliminary guidelines for consideration when a construction of an Icestupa for water storage is envisaged.

2 STUDY SITES

To accurately estimate and validate the ice volume of AIR the model requires three kinds of datasets namely, weather, water and ice volume. So through the winters of 2019, 2020 and 2021 several scientific AIR were constructed by teams in Switzerland and India. Each site had an Automatic Weather Station (AWS) nearby. Also drone flights were conducted periodically to record AIR ice volume. For this analysis, we have chosen 4 of the AIR which have a relatively complete dataset associated with them.

2.1 Construction

The construction strategy used in each site varied. CH20 and CH21 AIR was constructed by Guttannen Bewegt Association on a garden adjacent to a stream in Guttannen, Switzerland. To initiate the ice formation process, tree branches were laid covering the fountain pipe. The fountain height varied between 2 to 5 m during the construction period. Fountain operation was guided by temperature conditions.

The IN21 AIR was constructed as part of the Icestupa Competition in Gangles, Ladakh, India. It was constructed adjacent to another AIR and merged with it. To initiate the ice formation process, a dome of 2 m radius was constructed and the fountain pipeline was erected at the center using a tripod. Fountain operation was interrupted only due to pipeline freezing events. The fountain height varied between 5 to 9 m.

The CH19 AIR was constructed by the Eispalast in Schwarzsee, Switzerland. It was contained inside a wooden boundary adjacent to a stream. Fountain operation was guided by temperature conditions. The water spray of the fountain was initially adjusted so that most of the water droplets land within the wooden boundary zone. The ice formation was guided by adding a metal framework at the ice structure base after the first night of operation. Several cotton threads were tied between the ice structure base and fountain pole for accelerating and further guiding the ice formation process.

2.2 Measurements

2.2.1 Weather measurements

Air temperature, relative humidity, wind speed, pressure, longwave, shortwave direct and diffuse radiation are required to calculate the surface energy balance of an AIR. All the 4 sites had AWS near the construction site which measured most of these parameters. The specific corrections applied on the input dataset for each site is described in the Appendix. In addition, we used ERA5 reanalysis dataset (Copernicus Climate Change Service (C3S), 2017) for filling data gaps and adding data that were not measured directly at the respective site. The ERA5 reanalysis dataset has a good correlation with lower elevation sites in Switzerland (Scherrer, 2020) but a poor correlation for the Indian (IN21) site. So the weather dataset for the IN21 site was completed using another AWS nearby as described in the Appendix.

2.2.2 Discharge measurements

The water flow rate or discharge was measured via an ultrasonic sensor attached to the fountain supply pipeline for all the sites. However, due to various malfunctions, the discharge measurements were incomplete for all the sites except CH19. Using the hourly webcam images of the CH sites, the discharge duration was determined. The available discharge measurement was later used to determine the

93 average discharge quantity during these periods. For the IN21 site, discharge duration was estimated by
 94 manual observations and discharge quantity was arbitrarily set to be 60 l/min .

95 2.2.3 Ice volume measurements

96 Several Drone flights were conducted in every AIR site. The DEM generated through these flights were
 97 analysed to obtain the circumference and volume of the ice structure. The mean circumference measured
 98 during the fountain duration was set as the spray radius (r_{spray}) and the first drone flight was used to set
 99 the dome volume (V_{dome}) for model initialisation. The ice volume data was later used for calibration and
 100 validation of the model. There were no drone flights conducted for CH19 AIR, so the r_{spray} was instead
 101 calculated from fountain attributes as described in Appendix.

AIR	Gangles, 2021	Guttannen, 2021	Guttannen, 2020	Schwarzsee, 2019
Code	IN21	CH21	CH20	CH19
Altitude [m a.s.l.]	4025	1047	1047	967
Fountain Duration	Jan 18 - Mar 10	Nov 22 - Feb 21	Jan 3 - Feb 27	Jan 30 - Feb 16
Drone Flights	6	9	3	0
r_{spray} [m]	10.8	6.9	7.7	1.2
V_{dome} [m^3]	78.5	13.2	23.9	0

102 103 The model application is restricted to CH21 AIR below. Model results and figures for other AIR can be
 104 found in the supplementary materials.

3 MODEL SETUP

105 106 A bulk energy and mass balance model is used to calculate the amounts of ice, meltwater, water vapour
 107 and runoff water of the AIR every hour. This model consists of four modules which estimates the AIR, a)
 108 geometric evolution , b) energy balance, c) surface temperature and d) mass balance.

108 3.1 Geometric evolution

109 110 Radius r_{ice}^i and height h_{ice}^i define the dimensions of the AIR assuming its geometry to be a cone. The
 surface area A^i exposed to the atmosphere and volume V^i are:

$$A = \pi \cdot r_{ice} \cdot \sqrt{r_{ice}^2 + h_{ice}^2} \quad (1)$$

$$V = \pi/3 \cdot r_{ice}^2 \cdot h_{ice} \quad (2)$$

111 112 Note that we do not specify the time step superscript i of the shape variables A , V , r_{ice} and h_{ice} for
 113 brevity. The equations used henceforth display model time step superscript i only if it is different from the
 current time step.

114 With the mass of the AIR M_{ice} , its current volume can also be expressed as:

$$V = M_{ice}/\rho_{ice} \quad (3)$$

115 where ρ_{ice} is the density of ice (917 kg m^{-3}).

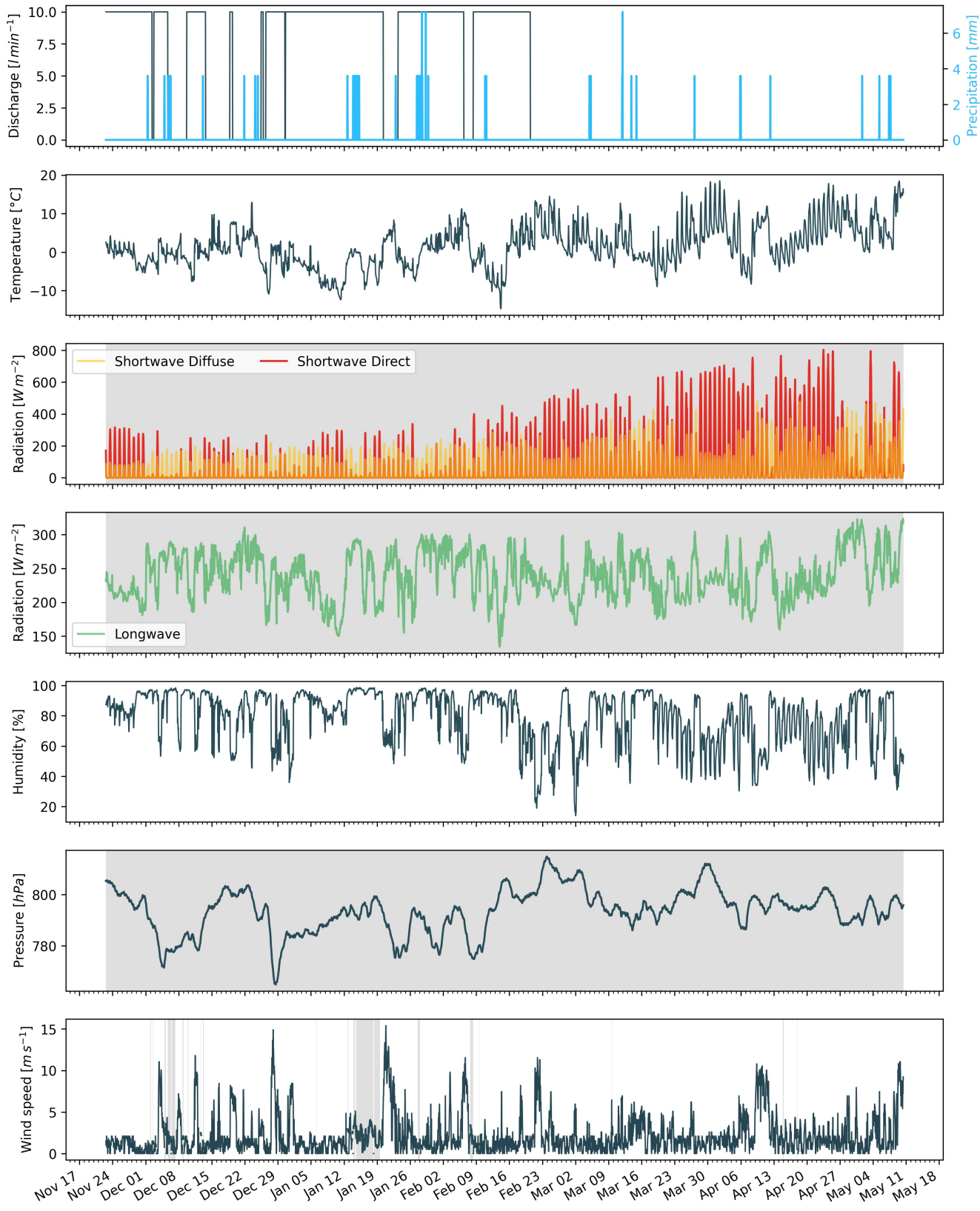


Figure 2. Measurements at the AWS of CH21 were used as main model input data in hourly frequency. Missing data, data gaps and errors were filled from the ERA5 dataset (shaded regions).

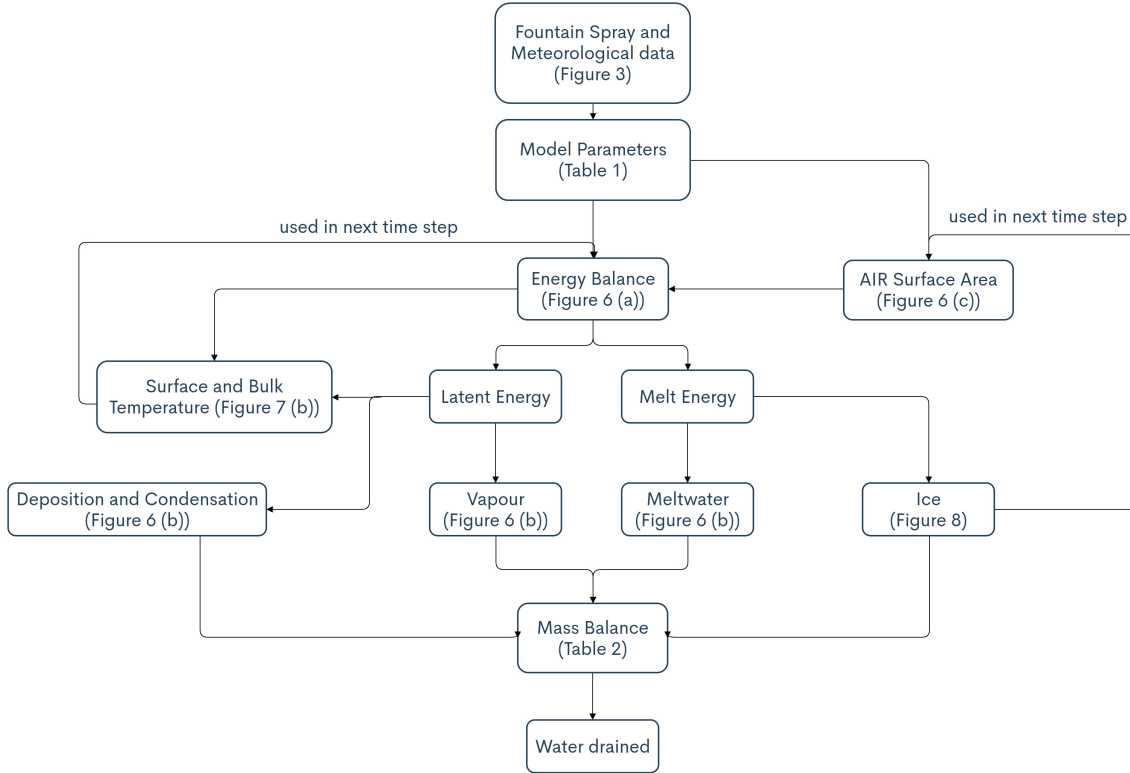


Figure 3. Model schematic showing the algorithm used in the model at every time step. Further details about the variables can be found in the associated tables and figures.

116 The influence of the AIR fountain is parameterised by the fountain water temperature T_w and its spray
 117 radius r_{spray} . The initial radius r_0 of the AIR is assumed to be r_{spray} . The initial height h_0 depends on the
 118 dome volume V_{dome} used to construct the AIR as follows:

$$h_0 = \Delta x + \frac{3 \cdot V_{dome}}{\pi r_{spray}^2} \quad (4)$$

119 where Δx is the surface layer thickness (defined in Section 3.2)

120 During subsequent time steps, the dimensions of the AIR evolve assuming a uniform ice formation and
 121 decay across its surface area with an invariant slope $s_{cone} = \frac{h_{ice}}{r_{ice}}$. During these time steps, the volume is
 122 parameterised using Eqn. 2 as:

$$V = \frac{\pi \cdot r_{ice}^3 \cdot s_{cone}}{3} \quad (5)$$

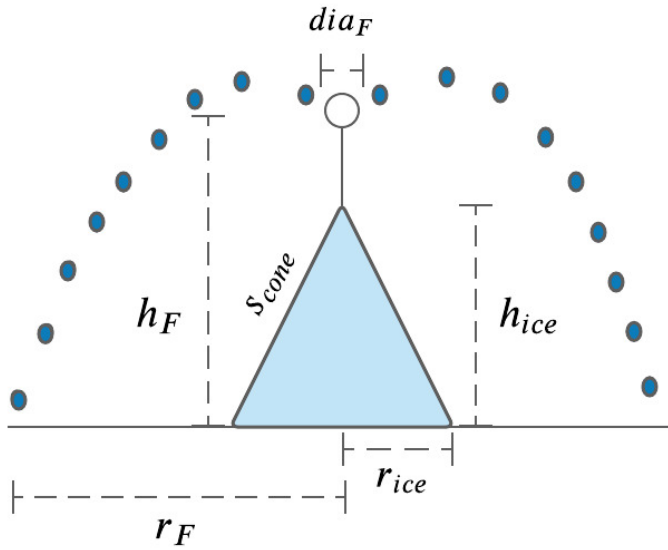


Figure 4. Shape variables and fountain constants of the CH21 Icestupa. r_{ice} is the radius, h_{ice} is the height and s_{cone} is the slope of the ice cone. r_{spray} is the spray radius, h_F is the height and dia_F is the nozzle diameter of the fountain.

123 However, the Icestupa cannot outgrow the maximum range of the water droplets ($(r_{ice})_{max} = r_F$).
 124 Combining equations 2, 4, 3 and 5, the geometric evolution of the Icestupa at each time step i can be
 125 determined by considering the following rules:

$$(r_{ice}, h_{ice}) = \begin{cases} (r_{spray}, h_0) & \text{if } i = 0 \\ (r_{ice}^{i-1}, \frac{3 \cdot M_{ice}}{\pi \cdot \rho_{ice} \cdot (r_{ice}^{i-1})^2}) & \text{if } r_{ice}^{i-1} \geq r_F \text{ and } \Delta M_{ice} > 0 \\ (\frac{3 \cdot M_{ice}}{\pi \cdot \rho_{ice} \cdot s_{cone}})^{1/3} \cdot (1, s_{cone}) & \text{otherwise} \end{cases} \quad (6)$$

126 where $\Delta M_{ice} = M_{ice}^{i-1} - M_{ice}^{i-2}$

127 3.2 Energy Balance

128 The energy balance equation (Hock, 2005) for the AIR is formulated as follows:

$$q_{SW} + q_{LW} + q_L + q_S + q_F + q_G = q_{surf} \quad (7)$$

129 where q_{surf} is the surface energy flux in $[W m^{-2}]$; q_{SW} is the net shortwave radiation; q_{LW} is the net
 130 longwave radiation; q_L and q_S are the turbulent latent and sensible heat fluxes. q_F represents the heat
 131 exchange of the fountain water droplets with the AIR ice surface. q_G represents ground heat flux between
 132 Icestupa surface and Icestupa interior. Energy transferred in the direction of the ice surface is always
 133 denoted as positive and away as negative.

134 Equation 7 is usually referred to as the energy budget for “the surface”, but practically it must apply
 135 to a surface layer of ice with a finite thickness Δx . The energy flux acts upon the Icestupa surface layer
 136 which has an upper and a lower boundary defined by the atmosphere and the ice body of the Icestupa,
 137 respectively. The parameter selection for Δx is based on the following two arguments: (a) the ice thickness

138 Δx should be small enough to represent the surface temperature variations every model time step Δt and
 139 (b) Δx should be large enough for these temperature variations to not reach the bottom of the surface layer.
 140 Therefore, we introduced a 20 mm thick surface layer for a model time step of 1 hour, over which the
 141 energy balance is calculated. A sensitivity analysis was later performed to understand the influence of this
 142 factor. Here, we define the surface temperature T_{ice} to be the modelled average temperature of the Icestupa
 143 surface layer and the energy flux q_{surf} is assumed to act uniformly across the Icestupa area A .

144 3.2.1 Net Shortwave Radiation q_{SW}

145 The net shortwave radiation q_{SW} is computed as follows:

$$q_{SW} = (1 - \alpha) \cdot (SW_{direct} \cdot f_{cone} + SW_{diffuse}) \quad (8)$$

146 where SW_{direct} and $SW_{diffuse}$ are the ERA5 direct and diffuse short wave radiation, α is the modelled
 147 albedo and f_{cone} is the area fraction of the ice structure exposed to the direct shortwave radiation.

148 We model the albedo using a scheme described in Oerlemans and Knap (1998). The scheme records the
 149 decay of albedo with time after fresh snow is deposited on the surface. δt records the number of time steps
 150 after the last snowfall event. After snowfall, albedo changes over a time step, δt , as

$$\alpha = \alpha_{ice} + (\alpha_{snow} - \alpha_{ice}) \cdot e^{(-\delta t)/\tau} \quad (9)$$

151 where α_{ice} is the bare ice albedo value (0.35), α_{snow} is the snow ice albedo value (0.85) and τ is a decay
 152 rate, which determines how fast the albedo of the ageing snow reaches this value. The decay rate τ is
 153 assumed to have a base value of 10 days similar to values obtained by Schmidt et al. (2017) for wet surfaces
 154 and its maximal value is set based on observations by Oerlemans and Knap (1998) as shown in Table 1.
 155 Furthermore, the albedo α varies depending on the water source that formed the current Icestupa surface.
 156 Correspondingly, the albedo is reset to the value of bare ice albedo if the fountain is spraying water onto
 157 the current ice surface and to the value of fresh snow albedo if a snowfall event occurred. Snowfall events
 158 are assumed if the air temperature is below $T_{ppt} = 1^{\circ}C$ (Fujita and Ageta, 2000).

159 The area fraction f_{cone} of the ice structure exposed to the direct shortwave radiation depends on the
 160 shape considered. The direct solar radiation incident on the AIR surface is first decomposed into horizontal
 161 and vertical components using the solar elevation angle θ_{sun} . For a conical shape, half of the total curved
 162 surface is exposed to the vertical component of the direct shortwave radiation and the projected triangle
 163 of the curved surface is exposed to the horizontal component of the direct shortwave radiation. The solar
 164 elevation angle θ_{sun} used is modelled using the parametrisation proposed by Woolf (1968). Accordingly,
 165 f_{cone} is determined as follows:

$$f_{cone} = \frac{(0.5 \cdot r_{ice} \cdot h_{ice}) \cdot \cos\theta_{sun} + (\pi \cdot r_{ice}^2 / 2) \cdot \sin\theta_{sun}}{\pi \cdot r_{ice} \cdot (r_{ice}^2 + h_{ice}^2)^{1/2}} \quad (10)$$

166 The ERA5 diffuse shortwave radiation is assumed to impact the conical Icestupa surface uniformly.

167 3.2.2 Net Longwave Radiation q_{LW}

168 The net longwave radiation q_{LW} is determined as follows:

$$q_{LW} = LW_{in} - \sigma \cdot \epsilon_{ice} \cdot (T_{ice} + 273.15)^4 \quad (11)$$

169 where T_a represents the measured air temperature, T_{ice} is the modelled surface temperature, both
 170 temperatures are given in $^{\circ}\text{C}$, $\sigma = 5.67 \cdot 10^{-8} \text{ J m}^{-2} \text{ s}^{-1} \text{ K}^{-4}$ is the Stefan-Boltzmann constant, LW_{in}
 171 denotes the incoming longwave radiation derived from the ERA5 dataset and ϵ_{ice} is the corresponding
 172 emissivity value for the Icestupa surface (see Table 1).

173 3.2.3 Turbulent sensible q_S and latent q_L heat fluxes

174 The turbulent sensible q_S and latent heat q_L fluxes are computed with the following expressions proposed
 175 by Garratt (1992):

$$q_S = c_a \cdot \rho_a \cdot p_a / p_{0,a} \cdot \frac{\kappa^2 \cdot v_a \cdot (T_a - T_{ice})}{(\ln \frac{h_{AWS}}{z_{ice}})^2} \quad (12)$$

$$q_L = 0.623 \cdot L_s \cdot \rho_a / p_{0,a} \cdot \frac{\kappa^2 \cdot v_a (p_{v,a} - p_{v,ice})}{(\ln \frac{h_{AWS}}{z_{ice}})^2} \quad (13)$$

176 where h_{AWS} is the measurement height above the ground surface of the AWS (in m), v_a is the wind
 177 speed in $[m \text{ s}^{-1}]$, c_a is the specific heat of air at constant pressure ($1010 \text{ J kg}^{-1} \text{ K}^{-1}$), ρ_a is the air density
 178 at standard sea level (1.29 kg m^{-3}), $p_{0,a}$ is the air pressure at standard sea level (1013 hPa), κ is the
 179 von Karman constant (0.4), L_s is the heat of sublimation (2848 kJ kg^{-1}) and z_{ice} (1.7 mm) denotes the
 180 roughness length of ice (momentum and scalar). The vapor pressures over air ($p_{v,a}$) and ice ($p_{v,ice}$) was
 181 obtained using the following formulation given in WMO (2018):

$$\begin{aligned} p_{v,a} &= 6.107 \cdot 10^{(7.5 \cdot T_a / (T_a + 237.3))} \\ p_{v,ice} &= (1.0016 + 3.15 \cdot 10^{-6} \cdot p_a - 0.074 \cdot p_a^{-1}) \cdot (6.112 \cdot e^{(22.46 \cdot T_{ice} / (T_{ice} + 272.62))}) \end{aligned} \quad (14)$$

182 where p_a is the measured air pressure in [hPa].

183 3.2.4 Fountain water heat flux q_F

184 The interaction between the fountain water and the ice surface is taken into account by assuming that
 185 the ice surface temperature remains constant at $0 \text{ }^{\circ}\text{C}$ during time steps when the fountain is active. This
 186 process can be divided into two simultaneous steps: (a) the water temperature T_{water} is cooled to $0 \text{ }^{\circ}\text{C}$
 187 and (b) the ice surface temperature is warmed to $0 \text{ }^{\circ}\text{C}$. Process (a) transfers the necessary energy for
 188 process (b) throughout the fountain runtime. We further assume that this process is instantaneous, i.e. the
 189 ice temperature is immediately set to $0 \text{ }^{\circ}\text{C}$ within just one time step Δt when the fountain is switched on.
 190 Thus, the heat flux caused by the fountain water is calculated as follows:

$$q_F = \begin{cases} 0 & \text{if } \Delta M_F = 0 \\ \frac{\Delta M_F \cdot c_{water} \cdot T_{water}}{\Delta t \cdot A} + \frac{\rho_{ice} \cdot \Delta x \cdot c_{ice} \cdot T_{ice}}{\Delta t} & \text{if } \Delta M_F > 0 \end{cases} \quad (15)$$

191 with c_{ice} as the specific heat of ice.

192 3.2.5 Bulk Icestupa heat flux q_G

193 The bulk Icestupa heat flux q_G corresponds to the ground heat flux in normal soils and is caused by the
 194 temperature gradient between the surface layer (T_{ice}) and the ice body (T_{bulk}). It is expressed by using the
 195 heat conduction equation as follows:

$$q_G = k_{ice} \cdot (T_{bulk} - T_{ice}) / l_{ice} \quad (16)$$

196 where k_{ice} is the thermal conductivity of ice ($2.123 \text{ W m}^{-1} \text{ K}^{-1}$), T_{bulk} is the mean temperature of the
 197 ice body within the Icestupa and l_{ice} is the average distance of any point in the surface to any other point in
 198 the ice body. T_{bulk} is initialised as 0°C and later determined from Eqn. 16 as follows:

$$T_{bulk}^{i+1} = T_{bulk} - (q_G \cdot A \cdot \Delta t) / (M_{ice} \cdot c_{ice}) \quad (17)$$

199 Since AIR's typically have conical shapes with $r_{ice} \gg h_{ice}$, we assume that the center of mass of the ice
 200 body is near the base of the fountain. Thus, the distance of every point in the AIR surface layer from the ice
 201 body's center of mass is between h_{ice} and r_{ice} . So we calculate q_G here assuming $l_{ice} = (r_{ice} + h_{ice})/2$.

202 **3.3 Surface temperature**

203 The available energy q_{surf} can act on the surface of the AIR to a) change its temperature, b) melt ice or
 204 c) freeze ice. So Eqn. 7 can be rewritten as:

$$q_{surf} = q_{freeze/melt} + q_T \quad (18)$$

205 where q_T , q_{freeze} and q_{melt} represent energy associated with process (a), (b) and (c) respectively.

206 To distribute the surface energy flux into these three components, we categorize the model time steps
 207 as freezing or melting events. Freezing events can only occur if there is fountain water available and the
 208 surface energy flux is negative. But just these two conditions are not sufficient as the latent heat energy
 209 can only contribute to temperature fluctuations. So to prevent latent heat energy from turning a melting
 210 event into a freezing event an additional condition namely $(q_{surf} - q_L) < 0$ is required. Thus, freezing and
 211 melting events are identified as follows:

$$q_{freeze/melt} = \begin{cases} q_{freeze} & \text{if } \Delta M_F > 0 \text{ and } q_{surf} < 0 \text{ and } (q_{surf} - q_L) < 0 \\ q_{melt} & \text{otherwise} \end{cases} \quad (19)$$

212 During a freezing event, the available energy $(q_{surf} - q_L)$ can either be sufficient or insufficient to
 213 freeze the fountain water available. If insufficient, the additional energy further cools down the surface
 214 temperature. So the surface energy flux distribution during a freezing event can be represented as:

$$(q_{freeze}, q_T) = \begin{cases} (q_{surf} - q_L, q_L) & \text{if } \Delta M_F \geq -\frac{(q_{surf} - q_L)A \cdot \Delta t}{L_f} \\ \left(\frac{\Delta M_F \cdot L_f}{A \cdot \Delta t}, q_{surf} + \frac{\Delta M_F \cdot L_f}{A \cdot \Delta t}\right) & \text{if } \Delta M_F < -\frac{(q_{surf} - q_L)A \cdot \Delta t}{L_f} \end{cases} \quad (20)$$

215 During a melting event, the surface energy flux (q_{surf}) is first used to change the surface temperature to
 216 T_{temp} calculated as:

Table 1. Free parameters in the model categorised as constant, uncertain and site parameters. Base value (B) and uncertainty (U) were taken from the literature. For assumptions (assum.), the uncertainty was chosen to be relatively large (5 %). For measurements (meas.), the uncertainty due to parallax errors is chosen to be (1 %).

Constant Parameters	Symbol	Value	References
Van Karman constant	κ	0.4	B: Cuffey and Paterson
Stefan Boltzmann constant	σ	$5.67 \cdot 10^{-8} W m^{-2} K^{-4}$	B: Cuffey and Paterson
Air pressure at sea level	$p_{0,a}$	1013 hPa	B: Mölg and Hardy
Density of water	ρ_w	$1000 kg m^{-3}$	B: Cuffey and Paterson
Density of ice	ρ_{ice}	$917 kg m^{-3}$	B: Cuffey and Paterson
Density of air	ρ_a	$1.29 kg m^{-3}$	B: Mölg and Hardy
Specific heat of ice	c_{ice}	$2097 J kg^{-1} ^\circ C^{-1}$	B: Cuffey and Paterson
Specific heat of water	c_w	$4186 J kg^{-1} ^\circ C^{-1}$	B: Cuffey and Paterson
Specific heat of air	c_a	$1010 J kg^{-1} ^\circ C^{-1}$	B: Mölg and Hardy
Thermal conductivity of ice	k_{ice}	$2.123 W m^{-1} K^{-1}$	B: Bonales et al.
Latent Heat of Sublimation	L_s	$2848 kJ kg^{-1}$	B: Cuffey and Paterson
Latent Heat of Fusion	L_f	$334 kJ kg^{-1}$	B: Cuffey and Paterson
Uncertain Parameters		Range	
Precipitation	T_{ppt}	$1 ^\circ C$	$\pm 1 ^\circ C$
Temperature threshold			B + U: Fujita and Ageta, Zhou et al.
Ice Emissivity	ϵ_{ice}	0.95	[0.949,0.993]
Ice Albedo	α_{ice}	0.35	$\pm 5 \%$
Snow Albedo	α_{snow}	0.85	$\pm 5 \%$
Albedo Decay Rate	τ	10 days	[1, 22] days
Surface layer thickness	Δx	20 mm	[1, 10] mm
Fountain Parameters		Range	
Spray Radius	r_{spray}		$\pm 5 \%$
Water temperature	T_{water}	$1 ^\circ C$	[0, 5] $^\circ C$

$$T_{temp} = \frac{q_{surf} \cdot \Delta t}{\rho_{ice} \cdot c_{ice} \cdot \Delta x} + T_{ice} \quad (21)$$

217 If $T_{temp} > 0^\circ C$, then energy is reallocated from q_T to q_{melt} to maintain surface temperature at melting
218 point. So the surface energy flux distribution during a melting event can be represented as:

$$(q_{melt}, q_T) = \begin{cases} (0, q_{surf}) & \text{if } T_{temp} < 0 \\ \left(\frac{T_{temp} \cdot \rho_{ice} \cdot c_{ice} \cdot \Delta x}{\Delta t}, q_{surf} - \frac{T_{temp} \cdot \rho_{ice} \cdot c_{ice} \cdot \Delta x}{\Delta t} \right) & \text{if } T_{temp} > 0 \end{cases} \quad (22)$$

219 3.4 Mass Balance

220 The mass balance equation for an AIR is represented as:

$$\frac{\Delta M_F + \Delta M_{ppt} + \Delta M_{dep}}{\Delta t} = \frac{\Delta M_{ice} + \Delta M_{water} + \Delta M_{sub} + \Delta M_{runoff}}{\Delta t} \quad (23)$$

221 where M_F is the discharge of the fountain; M_{ppt} is the cumulative precipitation; M_{dep} is the cumulative
 222 accumulation through water vapour deposition; M_{ice} is the cumulative mass of ice; M_{water} is the cumulative
 223 mass of melt water; M_{sub} represents the cumulative water vapor loss by sublimation and M_{runoff} represents
 224 the fountain discharge runoff that did not interact with the AIR. The LHS of equation 23 represents the rate
 225 of mass input and the RHS represents the rate of mass output for an AIR.

226 Precipitation input is calculated as shown in equation 24a where ρ_w is the density of water (1000
 227 $kg\ m^{-3}$), ppt is the measured precipitation rate in [$m\ s^{-1}$] and T_{ppt} is the temperature threshold below
 228 which precipitation falls as snow. Here, snowfall events were identified using T_{ppt} as $1^{\circ}C$. Snow mass
 229 input is calculated by assuming a uniform deposition over the entire circular footprint of the Icestupa.

230 The latent heat flux is used to estimate either the evaporation and condensation processes or sublimation
 231 and deposition processes as shown in equation 24b. During time steps at which surface temperature is
 232 below $0^{\circ}C$ only sublimation and deposition can occur, but if the surface temperature reaches $0^{\circ}C$,
 233 evaporation and condensation can also occur. As the differentiation between evaporation and sublimation
 234 (and condensation and deposition) when the air temperature reaches $0^{\circ}C$ is challenging, we assume
 235 that negative (positive) latent heat fluxes correspond only to sublimation (deposition), i.e. no evaporation
 236 (condensation) is calculated.

237 Since we have categorized every time step as a freezing and melting event, we can determine the meltwater
 238 and ice generated using the associated energy fluxes as shown in equations 24c and 24d. Having calculated
 239 all the other mass components the fountain wastewater generated every time step can be calculated using
 240 equation 24e.

$$\frac{\Delta M_{ppt}}{\Delta t} = \begin{cases} \pi \cdot r_{ice}^2 \cdot \rho_w \cdot ppt & \text{if } T_a < T_{ppt} \\ 0 & \text{if } T_a \geq T_{ppt} \end{cases} \quad (24a)$$

$$\left(\frac{\Delta M_{dep}}{\Delta t}, \frac{\Delta M_{sub}}{\Delta t} \right) = \begin{cases} \frac{q_L \cdot A}{L_s} \cdot (1, 0) & \text{if } q_L \geq 0 \\ \frac{q_L \cdot A}{L_s} \cdot (0, -1) & \text{if } q_L < 0 \end{cases} \quad (24b)$$

$$\frac{\Delta M_{water}}{\Delta t} = \frac{q_{melt} \cdot A}{L_f} \quad (24c)$$

$$\frac{\Delta M_{ice}}{\Delta t} = \frac{q_{freeze} \cdot A}{L_f} + \frac{\Delta M_{ppt}}{\Delta t} + \frac{\Delta M_{dep}}{\Delta t} - \frac{\Delta M_{sub}}{\Delta t} - \frac{\Delta M_{melt}}{\Delta t} \quad (24d)$$

$$\frac{\Delta M_{runoff}}{\Delta t} = \frac{\Delta M_F - \Delta M_{ice}}{\Delta t} \quad (24e)$$

241 Considering AIRs as water reservoirs, we can quantify their potential through the amount of water they
 242 store (storage quantity) and the length of time they store it (storage duration). Another means of comparing
 243 different Icestupas is through their water storage efficiency defined accordingly as:

$$\text{Storage Efficiency} = \frac{M_{water}}{(M_F + M_{ppt} + M_{dep})} \cdot 100 \quad (25)$$

4 MODEL RESULTS

244 The model was forced with meteorological data from 22nd November to 10th May 2021 (Fig. 2) and
245 various parameters (see Table 1) to calculate the mass and energy balance of the CH21 AIR.

246 4.1 Energy and mass balance calculation

247 Daily averages of some components of the energy balance are shown in Fig. 5 (b). On average during
248 the experiment duration, the total energy balance was almost zero. Net shortwave radiation (35 W m^{-2}),
249 sensible (41 W m^{-2}) and latent heat flux (2 W m^{-2}) with a mostly positive flux towards the surface of the
250 icestupa were compensated by the net longwave radiation (- 47 W m^{-2}), the fountain water heat flux (-
251 13 W m^{-2}) and the freeze/melt energy (- 19 W m^{-2}). The contributions of other fluxes were negligible in
252 comparison.

253 Net shortwave radiation is the main input to, and the most varying energy flux on the ice surface. Its
254 variability is controlled by the surface albedo α and the area fraction f_{cone} which therefore represent key
255 variables in the energy balance (Fig. 6 (b)). Although global radiation flux reached a daily maximum value
256 of 340 W m^{-2} , q_{SW} only went up to 114 W m^{-2} . This is caused by the fact that less than 40 % of the direct
257 solar radiation influenced the Icestupa surface as shown by the area fraction f_{cone} in Fig. 6 (a). Snowfall is
258 the atmospheric variable connected most closely and proportionally to albedo. Higher and/or more frequent
259 snowfall thus decreases the energy available for melt due to the corresponding increase in α .

260 q_{LW} was predominantly negative indicating that this energy balance component drove the freezing of
261 the ice structure. Daily values of q_{LW} ranged from - 101 to 19 W m^{-2} . Turbulent sensible heat flux q_S
262 contributed mostly to the melt of the ice structure. Daily values of q_S ranged from - 3 to 410 W m^{-2} . Daily
263 values of the turbulent latent heat flux q_L ranged from - 90 to 157 W m^{-2} . Since the mean of q_L was positive,
264 the Icestupa gained mass cumulatively from the atmosphere due to the deposition process. Daily values
265 of fountain water heat flux ranged from - 119 to 4 W m^{-2} . q_F was also a significant contributor to the
266 freezing process like q_{LW} . So the influence of the fountain on the energy balance and the freezing events
267 was significant. The contribution of heat flux by conduction q_G was minimal as it only varied between
268 - 1 to 3 W m^{-2} with a mean of 0 W m^{-2} . The energy contributing to surface temperature changes (q_T)
269 was insignificant in comparison to the energy spent on freezing and melting ($q_{freeze/melt}$). The resulting
270 bulk temperature and the surface temperature are shown in Fig. 6 (b). For the total considered period,
271 $q_{freeze/melt}$ accounted for 30% of overall energy turnover. The energy turnover is calculated as the sum of
272 energy fluxes in absolute values. q_{LW} accounted for 22%, followed by q_S (20%), q_{SW} (16%), q_L (5%), q_F
273 (6%), q_T (1%) and q_G (0%).

274 Fig. 5 (c) represents the mass fluxes associated with these energy exchanges expressed in m w.e. It shows
275 the ice and meltwater formed due to q_{melt} , snow accumulated due to precipitation, water vapour deposition
276 and sublimation due to q_L .

277 The total water used for the Icestupa development includes contributions from the fountain (96.7%),
278 snowfall (2.9 %), deposition (0.5 %) as shown in Table 2. Therefore, in the case of CH21 we used a water
279 input of 1,034,328 kg, with a resultant storage efficiency of 19 %.

5 DISCUSSION

280 5.1 Important assumptions

281 In the sensitivity and uncertainty analysis presented above, we did not account for several general
282 assumptions and parametrisation choices that may cause model errors. Some assumptions and their
283 potential to cause errors are discussed below.

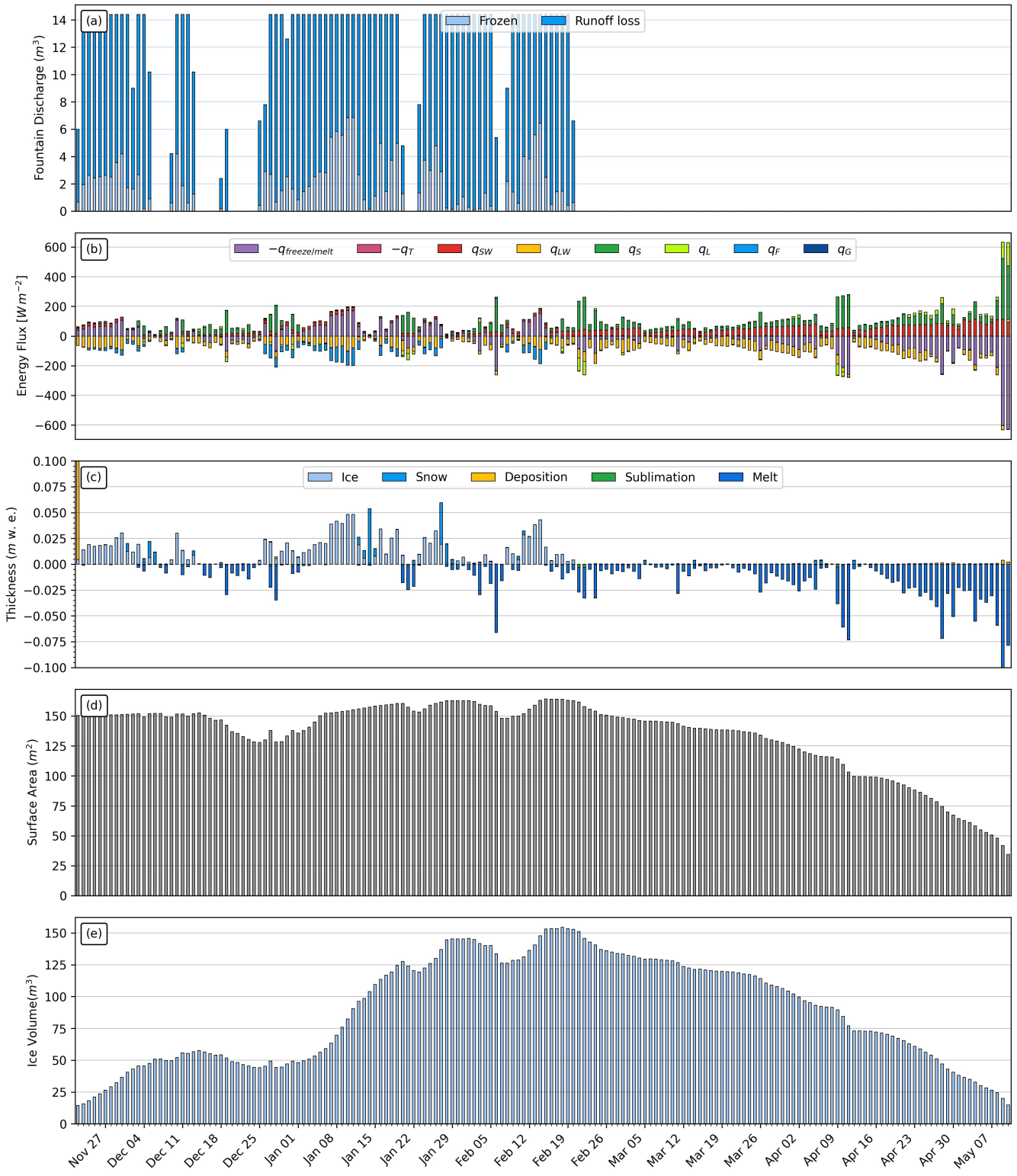


Figure 5. (a) Fountain discharge (b) energy flux components, (c) mass flux components (d) surface area and (e) volume of the Icestupa in daily time steps. q_{SW} is the net shortwave radiation; q_{LW} is the net longwave radiation; q_L and q_S are the turbulent latent and sensible heat fluxes. q_F represents the interactions of the fountain water with the AIR surface layer. q_G quantifies the heat conduction process between the AIR surface layer and the ice body.

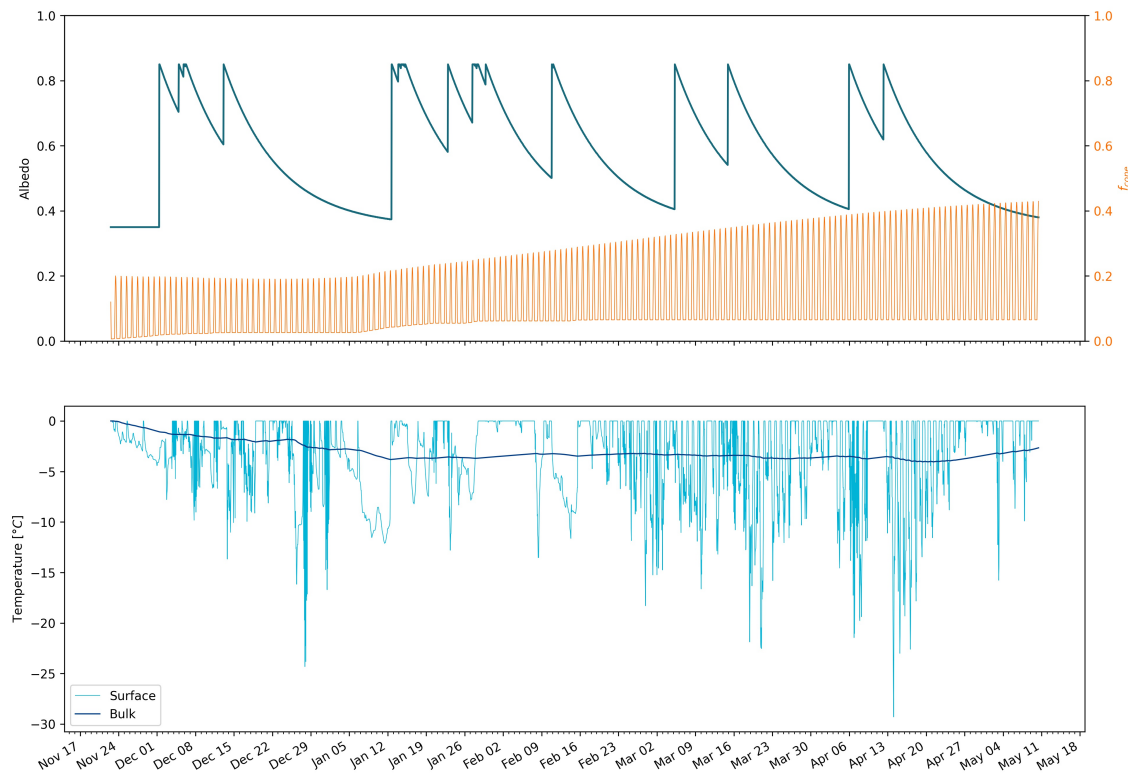


Figure 6. Some derived parameters of the model, namely, albedo and f_{cone} (a), Surface and bulk temperature (b). In (a), the green curve shows how snow and fountain-on events reset albedo between ice albedo and snow albedo. The decay of the snow albedo to ice albedo can also be observed. The orange curve shows how the solar radiation area fraction varied diurnally with variations in the solar elevation angle. In (b), the surface temperature (light blue curve) was forced to be 0°C during fountain activity. The corresponding bulk temperature is shown with the dark blue curve.

Table 2. Summary of mass balance components for the CH21 AIR at the end of the model run on 10th May 2021.

	Mass Component	Model ends
Input	M_F	1,000,041 kg
	M_{ppt}	29,533 kg
	M_{dep}	4,755 kg
Output	M_{water}	196,011 kg
	M_{ice}	12,304 kg
	M_{sub} M_{runoff}	4,747 kg 821,267 kg

- 284 • Turbulent Sensible and Latent Heat Fluxes: The method used to calculate the turbulent heat fluxes
 285 by Garratt (1992) assumes that the turbulent heat fluxes are acting over a uniform planar surface to
 286 determine the roughness length. Since our application is on a conical surface, the distance to the ice
 287 surface is not uniform and well defined. Hence, z_{ice} has no real physical significance here.

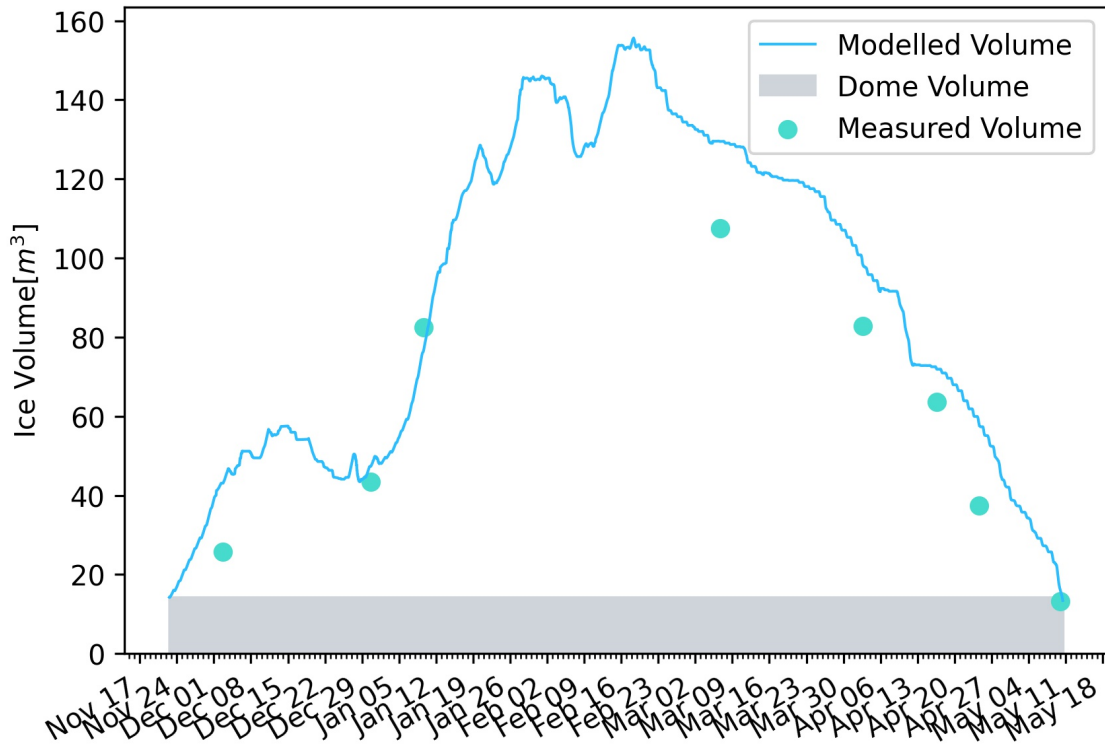


Figure 7. Modelled ice volume during the lifetime of the CH21 AIR (blue curve). Green points indicate the validation measurements.

- Droplet flight time loss: Water losses during the flight time of fountain droplets were neglected making all the fountain spray available for freezing. For the CH21 experiment, inclusion of this parameter does not influence results since it is already accounted for in the runoff water discharge rate which was at least $3 l \text{ min}^{-1}$.
- Nucleation of droplets: Corresponding to droplet flight time, ice/snow formation is also possible before surface contact if nucleation occurs during flight time. For the CH21 experiment, this process will further increase the freeze rate and hence the storage efficiency. This process is neglected for model simplicity.
- Shape Effects: The suppression of heat exchange between the snow/ice surface and the air adjacent to the surface effectively slows down snow/ice ablation in spring and promotes the stagnation of the cold air within topographical depressions (Fujita et al., 2010). The quantitative contribution of the atmospheric decoupling over melting snow/ice for the total mass and energy balance is ignored in the model.

6 APPENDIX

301 6.1 Ladakh Icestupa 2014/15

302 A 20 m tall Icestupa (Wangchuk, 2015c) was built in Phyang village, Ladakh at an altitude of 3500
 303 m a.s.l. Assuming a conical shape with a diameter of 20 m, the corresponding volume of this Icestupa
 304 becomes $2093 m^3$ or $1,920 m^3$ w.e. The fountain sprayed water at a rate of $210 l \text{ min}^{-1}$ (Wangchuk,
 305 2015e) from 21st January (Wangchuk, 2015a) to at least until 5th March 2015 (Wangchuk, 2015b) (around
 306 43 nights). Assuming fountain spray was active for 8 hours each night, we estimate water consumption to

307 be around $4,334\text{ m}^3$. Thus, during the construction/freezing period of the Icestupa, roughly 56 % of the
 308 water provided was wasted. The actual water loss is bound to be much higher due to further vapour losses
 309 during the melting period. This Icestupa completely melted away on 6th July 2015 (Wangchuk, 2015d).
 310 Therefore, the storage duration was 166 days or roughly 5 months.

311 6.2 Fountain spray radius of CH19 AIR

312 This fountain spray radius is determined by modelling the projectile motion of the water droplets. Using
 313 mass conservation, the droplet speed v_F can be determined from the spray rate d_F and the diameter dia_F
 314 of the nozzle as follows:

$$v_F = \frac{d_F}{\pi \cdot dia_F^2 / 4} \quad (26)$$

315 Afterwards, we assume that the water droplets move with an air friction free projectile motion from
 316 the fountain nozzle with a height h_F to the ice/ground surface. The resulting spray radius r_F was then
 317 determined from the projectile motion equation as follows:

$$r_F = \frac{v_F \cdot \cos\theta_F (v_F \cdot \sin\theta_F + \sqrt{(v_F \cdot \sin\theta_F)^2 + 2 \cdot g \cdot h_F})}{g} \quad (27)$$

318 where $g = 9.8\text{ ms}^{-2}$ is the acceleration due to gravity and $\theta_F = 45^\circ$ is the angle of launch.

REFERENCES

- 319 Apel, H., Abdykerimova, Z., Agalhanova, M., Baimaganbetov, A., Gavrilenco, N., Gerlitz, L., et al. (2018).
 320 Statistical forecast of seasonal discharge in central asia using observational records: development of a
 321 generic linear modelling tool for operational water resource management. *Hydrology and Earth System
 322 Sciences* 22, 2225–2254. doi:10.5194/hess-22-2225-2018
- 323 Bonales, L. J., Rodriguez, A. C., and Sanz, P. D. (2017). Thermal conductivity of ice prepared under
 324 different conditions. *International Journal of Food Properties* 20, 610–619. doi:10.1080/10942912.
 325 2017.1306551
- 326 Buytaert, W., Moulds, S., Acosta, L., Bievre, B. D., Olmos, C., Villacis, M., et al. (2017). Glacial melt
 327 content of water use in the tropical andes. *Environmental Research Letters* 12, 114014. doi:10.1088/
 328 1748-9326/aa926c
- 329 Chen, Y., Li, W., Deng, H., Fang, G., and Li, Z. (2016). Changes in central asia's water tower: Past, present
 330 and future. *Nature* doi:10.1088/1748-9326/aa926c
- 331 [Dataset] Copernicus Climate Change Service (C3S) (2017). Era5: Fifth generation ecmwf atmospheric
 332 reanalyses of the global climate. [Available at [https://cds.climate.copernicus.eu/
 333 cdsapp#!/home](https://cds.climate.copernicus.eu/cdsapp#!/home), accessed 2019-10-01]
- 334 Cuffey, K. M. and Paterson, W. S. B. (2010). *The Physics Of Glaciers* (Elsevier)
- 335 Fujita, K. and Ageta, Y. (2000). Effect of summer accumulation on glacier mass balance on the
 336 tibetan plateau revealed by mass-balance model. *Journal of Glaciology* 46, 244–252. doi:10.3189/
 337 172756500781832945
- 338 Fujita, K., Hiyama, K., Iida, H., and Ageta, Y. (2010). Self-regulated fluctuations in the ablation of a snow
 339 patch over four decades. *Water Resources Research* 46, W11541. doi:10.1029/2009WR008383
- 340 Garratt, J. R. (1992). *The Atmospheric Boundary Layer* (Cambridge University Press)

- 341 Grossman, D. (2015). As himalayan glaciers melt, two towns face the fallout [Available at
342 [https://e360.yale.edu/features/as_himalayan_glaciers_melt_two_towns_](https://e360.yale.edu/features/as_himalayan_glaciers_melt_two_towns_face_the_fallout)
343 [face_the_fallout](#), accessed 2019-10-01]
- 344 Hock, R. (2005). Glacier melt: a review of processes and their modelling. *Progress in Physical Geography: Earth and Environment* 29, 362–391
- 346 Hock, R., Rasul, G., Adler, C., Cáceres, B., Gruber, S., Hirabayashi, Y., et al. (2019). 2019: High mountain
347 areas. *IPCC Special Report on the Ocean and Cryosphere in a Changing Climate* [H.-O. Pörtner, D.C.
348 Roberts, V. Masson-Delmotte, P. Zhai, M. Tignor, E. Poloczanska, K. Mintenbeck, A. Alegría, M. Nicolai,
349 A. Okem, J. Petzold, B. Rama, N.M. Weyer (eds.)]
- 350 Hoelzle, M., Barandun, M., Bolch, T., Fiddes, J., Gafurov, A., Muccione, V., et al. (2019). *The status and
351 role of the alpine cryosphere in Central Asia*. doi:10.4324/9780429436475-8
- 352 Hori, M., Aoki, T., Tanikawa, T., Motoyoshi, H., Hachikubo, A., Sugiura, K., et al. (2006). In-situ
353 measured spectral directional emissivity of snow and ice in the 8–14 micrometer atmospheric window.
354 *Remote Sensing of Environment* 100, 486 – 502
- 355 Immerzeel, W. W., Lutz, A. F., Andrade, M., Bahl, A., Biemans, H., Bolch, T., et al. (2019). Importance
356 and vulnerability of the world's water towers. *Nature* 577, 364 – 369. doi:10.1038/s41586-019-1822-y
- 357 Mölg, T. and Hardy, D. R. (2004). Ablation and associated energy balance of a horizontal glacier surface
358 on kilimanjaro. *J. Geophys. Res.-Atmos.* 109, 1–13. doi:10.1029/2003JD004338
- 359 Nüsser, M., Dame, J., Kraus, B., Baghel, R., and Schmidt, S. (2019a). Socio-hydrology of artificial glaciers
360 in ladakh, india: assessing adaptive strategies in a changing cryosphere. *Regional Environmental Change*
361 doi:10.1007/s10113-018-1372-0
- 362 Nüsser, M., Dame, J., Parveen, S., Kraus, B., Baghel, R., and Schmidt, S. (2019b). Cryosphere-Fed
363 Irrigation Networks in the Northwestern Himalaya: Precarious Livelihoods and Adaptation Strategies
364 Under the Impact of Climate Change. *Mountain Research and Development* 39. doi:10.1659/
365 MRD-JOURNAL-D-18-00072.1
- 366 Oerlemans, J. and Knap, W. H. (1998). A 1 year record of global radiation and albedo in the
367 ablation zone of morteratschgletscher, switzerland. *Journal of Glaciology* 44, 231–238. doi:10.
368 3189/S0022143000002574
- 369 Scherrer, S. C. (2020). Temperature monitoring in mountain regions using reanalyses: lessons from the
370 alps. *Environmental Research Letters* 15, 044005
- 371 Schmidt, L. S., Aðalgeirs Þóttir, G., Guðmundsson, S., Langen, P. L., Pálsson, F., Mottram, R., et al. (2017).
372 The importance of accurate glacier albedo for estimates of surface mass balance on vatnajökull: evaluating
373 the surface energy budget in a regional climate model with automatic weather station observations. *The
374 Cryosphere* 11, 1665–1684. doi:10.5194/tc-11-1665-2017
- 375 Unger-Shayesteh, K., Vorogushyn, S., Farinotti, D., Gafurov, A., Duethmann, D., Mandychev, A., et al.
376 (2013). What do we know about past changes in the water cycle of central asian headwaters? a review.
377 *Global and Planetary Change* 110, 4 – 25. doi:10.1016/j.gloplacha.2013.02.004. Water in Central Asia
378 – Perspectives under global change
- 379 Wangchuk, S. (2014). Ice stupa artificial glaciers of ladakh [Available at www.indiegogo.com/projects/ice-stupa-artificial-glaciers-of-ladakh#/, accessed 2019-10-01]
- 380 Wangchuk, S. (2015a). The good news at ice stupa 24th january 2015 [Available at <http://icestupa.org/news/the-good-news-at-ice-stupa>, accessed 2019-10-01]
- 381 Wangchuk, S. (2015b). Ice stupa artificial glacier inaugurated
382 5th of march 2015 [Available at <http://icestupa.org/news/ice-stupa-artificial-glacier-inaugurated-5th-of-march>,
383 accessed 2019-10-01]

- 386 2019-10-01]
- 387 Wangchuk, S. (2015c). Ice stupa surpasses guiness world record [Available at <http://icestupa.org/news/ice-stupa-surpasses-guinness-world-record>, accessed 2019-10-01]
- 388 Wangchuk, S. (2015d). Ice stupa way of celebrating a special day [Available at <http://icestupa.org/news/ice-stupa-way-of-celebrating-a-special-day6th-of-ju>, accessed 2019-10-01]
- 389 Wangchuk, S. (2015e). World water day at ice stupa [Available at <http://icestupa.org/news/world-water-day-at-ice-stupa>, accessed 2019-10-01]
- 390 WMO (2018). *Guide to Instruments and Methods of Observation* (World Meteorological Organization ; 395 2018 (2018 Edition))
- 391 Woolf, H. M. (1968). *On the Computation of Solar Elevation Angles and the determination of sunrise and sunset times* (National Aeronautics and Space Administration)
- 392 Zhou, S., Kang, S., Gao, T., and Zhang, G. (2010). Response of zhadang glacier runoff in nam co basin, 393 tibet, to changes in air temperature and precipitation form. *Chinese Science Bulletin* 55, 2103–2110.
400 doi:10.1007/s11434-010-3290-5